Directional Distributions and Mean Square Slopes in the Equilibrium and Saturation Ranges of the Wave Spectrum

PAUL A. HWANG AND DAVID W. WANG

Oceanography Division, Naval Research Laboratory, Stennis Space Center, Mississippi

(Manuscript received 24 April 2000, in final form 28 August 2000)

ABSTRACT

Field observations show that the crosswind component constitutes a significant portion of the ocean surface mean square slope. The average ratio between the crosswind and upwind mean square slope components is 0.88 in slick-covered ocean surfaces. This large crosswind slope component cannot be explained satisfactorily based on our present models of a unimodal directional distribution function of ocean waves. Two-dimensional spectral analysis of the 3D ocean surface topography reveals that a bimodal directional distribution is a common feature for wave components shorter than the peak wavelength. The calculated result of the upwind and crosswind mean square slope components using a bimodal directional distributions yields substantial improvement in agreement with field measurements. Also discussed in this paper is the transition of the spectral function from an equilibrium form to a saturation form. Through comparison with the mean square slope data of the slick cases under which short waves are suppressed and calculation of the range of wavenumbers influenced by nonlinear wave–wave interaction, it is found that the transition from the equilibrium range to saturation range occurs at a wavenumber in the neighborhood of 6.5 times the peak wavenumber.

1. Introduction

Ocean surface waves are the roughness element of the air–water interface. The directional distribution of the ocean surface roughness is an important parameter in air–sea interaction studies and ocean remote sensing applications. Examples include magnitude and direction of energy and momentum fluxes between air and water, scatterometer wind velocity measurement, synthetic aperture radar imaging of the ocean wave field, and radar or optical detection of surface and subsurface features. The preferred representation of the ocean surface roughness properties is the directional wavenumber spectrum of the ocean waves. Such data have become available only recently. The results on the roughness wavenumber spectrum have emerged slowly because of difficulties in measurements and analyses. Several field measurements of wavenumber spectra of short waves (from several millimeters to several decimeters) obtained by scanning-laser slope sensing have been reported (e.g., Bock and Hara 1995; Hara et al. 1994, 1998; Hwang et al. 1996). In principle, scanning slope data include two orthogonal components of ocean surface slopes measured in the space domain. Detailed information on the directional distributions of individual spectral components of ocean waves can be derived from these measurements, but only limited results on the directional properties of short waves over a small range of wind speeds have been reported (Hwang 1995; Klinke and Jahne 1995; Hara et al. 1998).

Most ocean wave directional spectra are obtained from temporal measurements acquired by directional buoys (e.g., Longuet-Higgins 1963; Mitsuyasu et al. 1975; Hasselmann et al. 1973, 1980) or wave gauge arrays (e.g., Donelan et al. 1985). The transformation from frequency to wavenumber domain is carried out using the dispersion relationship. This approach is rather successful for long gravity waves. The application to shorter waves is not very satisfactory because of the large Doppler frequency shift caused by convection of short waves by surface currents. The large frequency shift introduces large uncertainties in the interpretation of the length scales of the measured (apparent) wave frequency (e.g., Phillips 1985; Hwang et al. 1996; Donelan et al. 1999).

For surface roughness investigations, the surface slope data of Cox and Munk (1954) remain the most comprehensive in terms of the range of wind speeds encountered and the extent of their statistical analysis. Based on their measurements, the ocean surface roughness has a significant crosswind component. In most cases, the ratio of the crosswind and upwind mean square slope components is

* U.S. Naval Research Laboratory Contribution Number JA/7332—00-0018

Corresponding author address: Dr. Paul A. Hwang, Oceanography Division, Naval Research Laboratory, Stennis Space Center, MS 39529-5004.
E-mail: paul.hwang@nrlssc.navy.mil

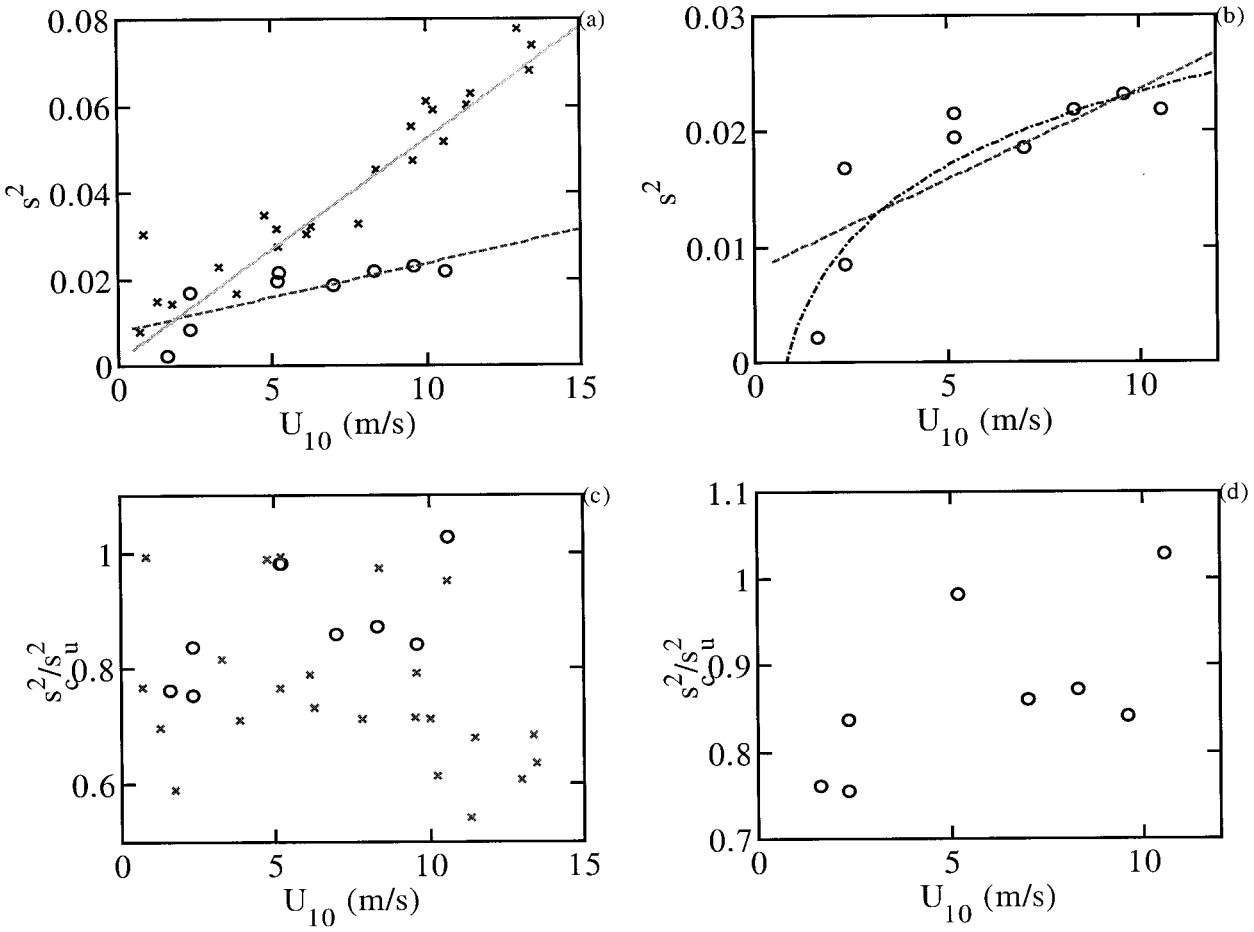

FIG. 1. The (a) sum and (c) ratio of the crosswind and upwind mean square slope components measured by Cox and Munk (1954). Circles are slick-covered conditions and crosses are clean surface conditions. Solid and dashed curves are their proposed linear wind dependence formulas [(1)–(2)]. For clarity, the slick cases are replotted in (b) and (d). The dashed–dotted curve in (c) is Phillips (1977) computation (7) based on a saturation spectrum (6) with $B = 4.6 \times 10^{-3}$.

greater than 0.7. The large crosswind to upwind ratio is also found in later measurements of high frequency ocean wave spectra using laser slope gauges (e.g., Hughes et al. 1977; Tang and Shemdin 1983; Hwang and Shemdin 1988). This ratio is much larger than what is expected from applying unimodal directional distribution functions currently established in the ocean wave spectral models.

Banner and Young (1994) emphasize that bimodality is a robust feature of the directional distribution of wind-generated waves. The dynamic process that produces a bimodal directional distribution is the nonlinear wave–wave interaction mechanism. Although bimodal directional distributions have been obtained from directional buoy data using analysis techniques such as the maximum entropy method (MEM) or maximum likelihood method (MLM) (Young 1994; Young et al. 1995; Ewans 1998; Wang and Hwang 2001), there remains uncertainty on the existence of directional bimodality, mainly because the quantitative results of bimodal directional distribution differ significantly depending on the processing method employed. The main difficulty of obtaining unambiguous directional resolution is due to the underdetermined measurements from directional buoys or wave gauge arrays: both systems provide estimations of a small number of directional moments for reconstructing the directional function, the number of degrees of freedom (dof) of which is essentially unlimited because the directional distribution is a continuous function of the wave propagation angle. As a result of underdetermined measurements, the resulting resolution of the surface wave directionality from directional buoys or wave gauge arrays is relatively limited. Hwang et al. (2000a,b) report 2D wavenumber spectral analysis of 3D surface topography measured by an airborne topographic mapper (ATM: an airborne scanning lidar system). The directional resolution derived from 3D topographic data is considerably better because the dof of the 3D measurements in the space domain is on the same order as the dof of the directional function in the angular domain. The analysis presented in Hwang et al. (2000b) illustrates that the directional resolution for a wave field generated by a steady 10 m s^{-1} wind field is better than 10° for wavenumber components higher than the peak

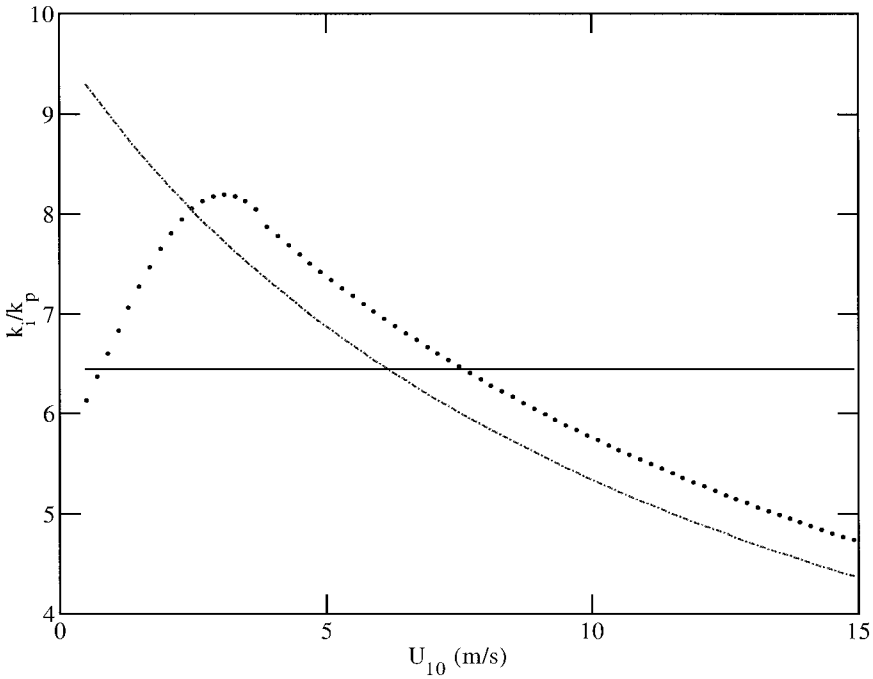

FIG. 2. Transition wavenumber separating the equilibrium and saturation ranges of the wave spectrum (13). Three different formulas of the drag coefficient are used. Solid curve: constant $C_d = 1.2 \times 10^{-3}$, dashed–dotted curve: Wu (1982), and dotted curve: Donelan (1990).

wavenumber. The directional spectra of the ATM data show clear directional bimodality (Hwang et al. 2000b). They also notice that cases of bimodal directional distributions are commonly found in the directional wavenumber spectra derived from similar 3D spatial measurements, such as those acquired by aerial stereo photography (Phillips 1958; Cote et al. 1960; Holthuijsen 1983), airborne imaging radar (Jackson et al. 1985) and land-based imaging radar (Wyatt 1995).

In this paper, we present computations of the upwind and crosswind mean square slope components using six different directional distribution models. These calculations are compared with Cox and Munk's (1954) measurements of the mean square slopes, which are briefly described in section 2. Because the measured mean square slope components are integrated over the full range of spectral components, sensitivity tests on key spectral parameters are investigated in section 3. Due to the fact that major uncertainties on the spectral properties in the short wave regime remain, we limit our investigation to gravity wave components in the equilibrium and saturation ranges of the spectrum. Quantitative results of the ratio of the crosswind and upwind slope components calculated using six directional distribution functions are presented in section 4. Further discussions on the spectral function and directional distributions are presented in section 5. A summary of the study is given in section 6.

2. Mean square slope data

The mean square slope results reported in Cox and Munk (1954) are derived from analyzing sun glitter patterns of the ocean surface obtained from an aircraft. The area of coverage for each image of glitter patterns is typically on the order of one-half square kilometer. The results, therefore, yield a high degree of statistical confidence. These data are shown in Figs. 1a and 1b. Based on these data, the total mean square slope of the ocean surface increases linearly with wind speed, and the following two formulas are given

for a clean surface:

$$s^2_{\text{clean}} = 5.12 \times 10^{-3}\, U + (3 \pm 4) \times 10^{-3} \qquad (1)$$

for a slick surface:

$$s^2_{\text{slick}} = 1.56 \times 10^{-3}\, U + (8 \pm 4) \times 10^{-3}. \qquad (2)$$

In (1) and (2), the wind velocity U is measured at a 12.5-m elevation. Combining their results with other later datasets and making corrections for cases that are affected by background swell, a slightly different formula is given in Hwang (1997) in terms of U_{10}, the neutral wind speed at 10-m elevation,

$$S^2_{\text{clean}} = 5.12 \times 10^{-3}\, U_{10} + 1.25 \times 10^{-3}, \qquad (3)$$

for a clean surface. The data of special interest to this paper are those collected from slick covered surfaces. Altogether, Cox and Munk (1954) report nine slick cases

(one natural slick and eight manmade slicks) with wind speeds ranging from 1.6 to 10.6 m s^{-1}. The ratio of crosswind and upwind components is quite large (Fig. 1d). For the nine slick cases, the mean value with one standard derivation is 0.88 $\pm$ 0.097, and none of the cases has a ratio less than 0.75. This large fraction of the crosswind mean square slope component has never been explained satisfactorily. As will be shown in section 4, calculations using established unimodal directional distribution functions underpredict the crosswind component considerably.

3. Spectral function

Cox and Munk (1954) calculated the damping of wave components due to the presence of surface slicks and reached the conclusion that, for the size of slicks employed in their experiments, waves shorter than 0.3 m are suppressed. The computational results compare satisfactorily with the Neumann spectral function available at that time. Phillips (1977) recalculated the mean square slope of slick covered cases using the saturation spectral function (Phillips 1958). Because waves longer than the peak wavelength make only an insignificant contribution to the surface slope, the total mean square slope can be computed by

$$s^2 = \int_{k_p}^{k_s} \chi_1(k)\, dk, \tag{4}$$

where the upper limit of integration, k_s, is the wavenumber above which the wave components are suppressed by the slick ($k_s = 2\pi/0.3$ rad m^{-1}); k_p is the peak wavenumber, defined by

$$k_p = \frac{g}{U_{10}^2}, \tag{5}$$

where g is the gravitational acceleration; and $\chi_1(k)$ is the slope spectrum, related to the displacement spectrum $\chi(k)$ by $\chi_1(k) = k^2\chi(k)$. By assuming a saturation spectrum of the form (Phillips 1958)

$$\chi(k) = Bk^{-3}, \tag{6}$$

Phillips (1977) shows that the mean square slopes of slick cases increase logarithmically with wind speed,

$$s^2 = B \ln\left(\frac{k_s U_{10}^2}{g}\right). \tag{7}$$

Equation (7) with $B = 4.6 \times 10^{-3}$, shown as the dashed–dotted curve in Fig. 1b, is in good agreement with the field results.

During the last two decades, field data suggest that the spectral function just above the spectral peak is more appropriately represented by an equilibrium spectral function of the form

$$\chi(k) = bu_* g^{-0.5} k^{-2.5}, \tag{8}$$

where b is a constant spectral coefficient with a mean value close to 5.2×10^{-2} (e.g., Phillips 1985; Hwang et al. 2000a) and u_* is the wind friction velocity. The upper-limit wavenumber for the equilibrium range has not been established. Phillips (1985) considers that suppression of short waves by surface drift currents is an important mechanism limiting the equilibrium range and suggests that the following expression for the upper-limit wavenumber, k_d, of the equilibrium spectrum,

$$k_d = r\frac{g}{u_*^2} = \frac{r}{C_d} k_p, \tag{9}$$

where r is a constant with a magnitude close to 0.3 (Phillips 1985, 523–525), and C_d is the drag coefficient, $C_d = u_*^2/U_{10}^2$.

There are several concerns about this upper limit. First, the range appears to be rather high. For $C_d = 1.2 \times 10^{-3}$ and $r = 0.3$, $k_d = 250k_p$. Second, the calculated total mean square slope is

$$s_d^2 = 2bC_d^{0.5}\left[\left(\frac{k_d}{k_p}\right)^{0.5} - 1\right]. \tag{10}$$

If k_d is indeed $O(250k_p)$, $(k_d/k_p)^{0.5} \gg 1$ inside the square-bracketed term on the right-hand side of (10), and

$$s_d^2 \approx 2bC_d^{0.5}\left(\frac{r}{C_d}\right)^{0.5} = 2br^{0.5}, \tag{11}$$

which is independent of wind speed! Furthermore, with $b = 5.2 \times 10^{-2}$ and $r = 0.3$, $s_d^2 = 0.057$, which is considerably larger than the field data (Fig. 1b).

We suggest that the classical concept of a saturation range (6) remains valid and that the range starts from the upper limit of the equilibrium range (8),

$$\chi(k) = \begin{cases} bu_* g^{-0.5} k^{-2.5}, & k \le k_i \\ Bk^{-3}, & k > k_i. \end{cases} \tag{12}$$

The transition wavenumber, k_i, separating the equilibrium and the saturation ranges can be calculated from matching the two branches in (12), that is, equating (6) and (8), which yields

$$k_i = \left(\frac{B}{b}\right)^2 \frac{1}{C_d} k_p. \tag{13}$$

For $B = 4.6 \times 10^{-3}$, $b = 5.2 \times 10^{-2}$, and $C_d = 1.2 \times 10^{-3}$, $k_i = 6.5k_p$. If different values of the spectral coefficients, B and b, are used, the ratio $m = k_i/k_p$ varies in proportion to $(B/b)^2$. The ratio m is also modified slightly if the drag coefficient is wind speed dependent. Figure 2 plots m as a function of U_{10} for three different formulas of the drag coefficient: one is constant (1.2×10^{-3}) and the other two are wind speed dependent (Wu 1982; Donelan 1990). In the wind speed range of the slick data ($U_{10} < 12$ m s^{-1}), the transition ratio m varies within the range of approximately 6.5 $\pm$ 2.

TABLE 1. The magnitude of $2bC_d^{0.5}(m^{0.5} - 1) - B\ln m$ as a function of m.

	m					
	4	5	6	7	8	9
$2bC_d^{0.5}(m^{0.5} - 1) - B\ln m$	-2.75×10^{-3}	-2.92×10^{-3}	-2.99×10^{-3}	-2.99×10^{-3}	-2.94×10^{-3}	-2.86×10^{-3}

The total mean square slopes integrated over the equilibrium and saturation ranges is

$$s_{es}^2 = [2bC_d^{0.5}(m^{0.5} - 1) - B\ln m] + B\ln\left(\frac{k_s}{g}\right) + 2B\ln U_{10}. \quad (14)$$

The first and second terms on the right-hand side of (14) are small. For example, with $b = 5.2 \times 10^{-2}$ and $B = 4.6 \times 10^{-3}$, the magnitude of the first term as a function of m is shown in Table 1. A constant friction coefficient, $C_d = 1.2 \times 10^{-3}$ is assumed for these calculations. For the assumption that waves shorter than 0.3 m are suppressed by slicks, $k_s \approx 20$ rad m^{-1} and $B\ln(k_s/g) = 3.28 \times 10^{-3}$. If $k_s \approx 30$ rad m^{-1} is assumed (waves shorter than 0.2 m are suppressed by the slick), $B\ln(k_s/g) = 5.15 \times 10^{-3}$. The sum of the first two terms on the right-hand side is, therefore, approximately $(0.3\sim2.3) \times 10^{-3}$. In all the following computations $k_s = 2\pi/0.3 = 20.9$ rad m^{-1} is used.

The logarithmic wind speed dependence is indicated in the last term of (14) and is in general agreement with the field data (Fig. 1b). Sensitivity of the mean square slope calculation on different formulas of the drag coefficient is shown in Fig. 3a, where curves for $C_d = 1.2 \times 10^{-3}$, and two wind-speed-dependent formulas of C_d (Wu 1982; Donelan 1990) are shown. For these computations $B = 4.6 \times 10^{-3}$ and $b = 5.2 \times 10^{-2}$ are used.

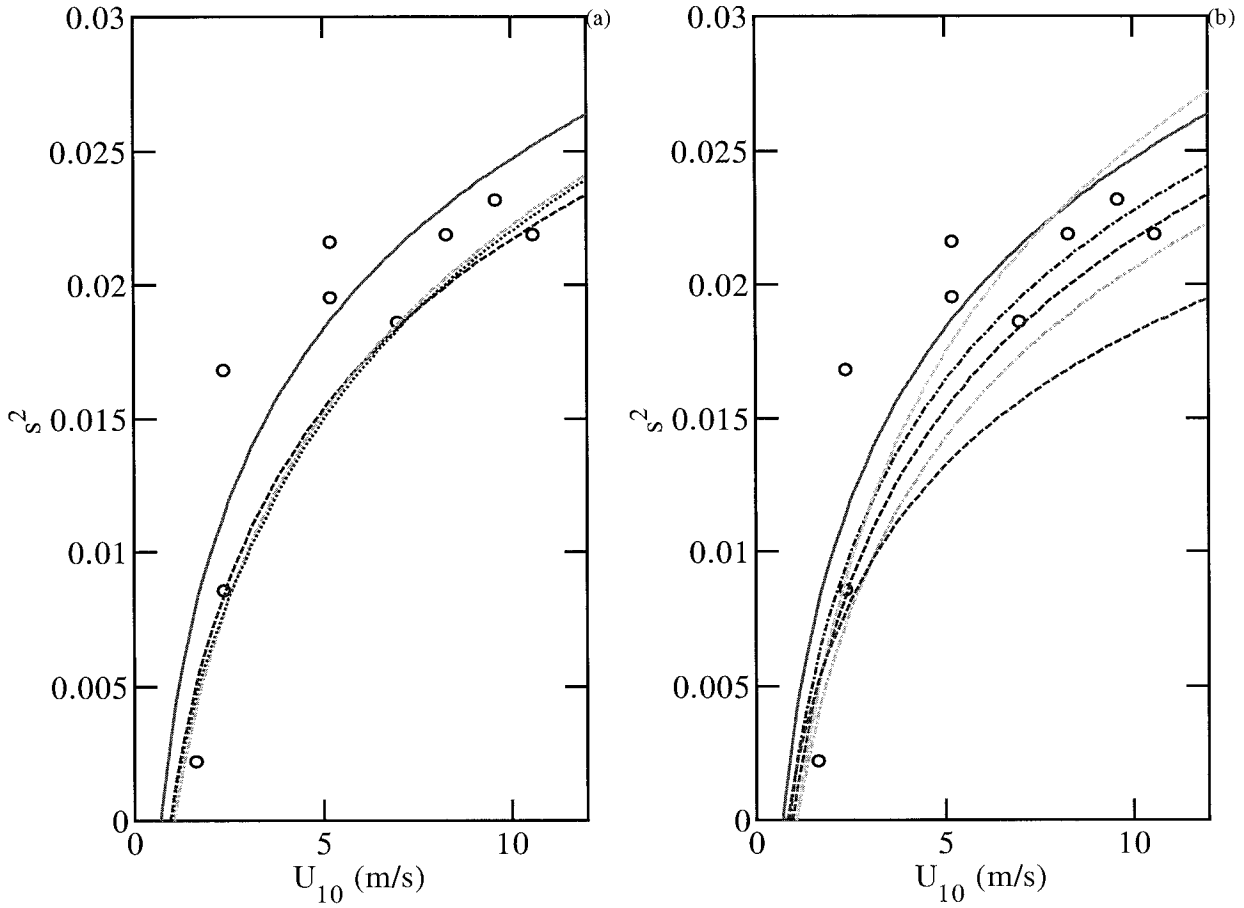

FIG. 3. Sensitivity test of various parameters on the calculation of mean square slopes. (a) Effects of the transition ratio, $m = k_i/k_p$, as a result of using different drag coefficient formulas. Dashed curve: $C_d = 1.2 \times 10^{-3}$, dashed-and-dotted curve: Wu (1982), and dotted curve: Donelan (1990). (b) Effects of the magnitudes of the spectral coefficients in the equilibrium and the saturation ranges. Dashed curves: $b = 5.2 \times 10^{-2}$, $B = [3.6, 4.6, 5.6] \times 10^{-3}$ and dashed-and-dotted curves: $B = 4.6 \times 10^{-3}$, $b = [4.2, 5.2, 6.2] \times 10^{-2}$. Higher spectral coefficient results in higher mean square slopes as expected. For reference, Phillips (1977) result (7) is shown with solid curves in both plots.

For reference, Phillips (1977) result described earlier (7) is also plotted. It is clear that, for the purpose of mean square slope calculation, the choice of different formulations of the drag coefficient is not important.

The magnitudes of the two spectral coefficients, B in the saturation range and b in the equilibrium range, obviously influence the quantitative result of the computation. Calculations with three different B values (3.6×10^{-3}, 4.6×10^{-3} and 5.6×10^{-3}) with $b = 5.2 \times 10^{-2}$ and three different b values (4.2×10^{-2}, 5.2×10^{-2} and 6.2×10^{-2}) with $B = 4.6 \times 10^{-3}$ are shown in Fig. 3b. In these calculations constant C_d (1.2×10^{-3}) and m (6.5) are used. Given that there are still considerable uncertainties on the spectral coefficients, the mean square slopes calculated from the proposed spectral function, with the equilibrium and saturation ranges defined by (12), are in very good agreement with the field data. In the following discussion of directional distributions and the ratio between crosswind and upwind mean square slope components, $B = 4.6 \times 10^{-3}$, $b = 5.2 \times 10^{-2}$, and C_d is calculated using the Donelan formula (1990).

4. Directional distributions and mean square slope components

For a given directional spectrum, $\chi(k, \theta) = \chi(k)D(k, \theta)$, the upwind and crosswind slope spectra can be expressed as

$$\chi_{1u}(k, \theta) = k_u^2 \chi(k) D(k, \theta) \quad \text{and} \tag{15}$$

$$\chi_{1c}(k, \theta) = k_c^2 \chi(k) D(k, \theta), \tag{16}$$

where subscripts u and c denote the upwind and crosswind components and $D(k, \theta)$ is the directional distribution function (assuming that the wind direction is at $\theta = 0$, thus $k_u = k \cos\theta$, and $k_c = k \sin\theta$). The ratio of crosswind and upwind mean square slope components integrated to an upper limit wavenumber, k_I, can be written as

$$r(k_I) = \frac{\displaystyle\int_{k_P}^{k_I} k^2 \chi(k) \left[\int_{-\pi}^{\pi} \sin^2\theta D(k, \theta)\, d\theta \right] dk}{\displaystyle\int_{k_p}^{k_I} k^2 \chi(k) \left[\int_{-\pi}^{\pi} \cos^2\theta D(k, \theta)\, d\theta \right] dk}. \tag{17}$$

For individual wavenumber components, the ratio is

$$d(k) = \frac{\displaystyle\int_{-\pi}^{\pi} \sin^2\theta D(k, \theta)\, d\theta}{\displaystyle\int_{-\pi}^{\pi} \cos^2\theta D(k, \theta)\, d\theta}. \tag{18}$$

Clearly, the specific functional form of the directional distribution plays an important role on the magnitudes of $r(k_I)$ and $d(k)$. Figure 4 shows six different directional distribution models reported in the literature. The calculation of $r(k_I)$ and $d(k)$ are carried out for the angular range $-\pi/2 \le \theta \le \pi/2$. The first three models (Mitsuyasu et al. 1975; Hasselmann et al. 1980; Donelan et al. 1985, with modification by Banner 1990) are unimodal (Figs. 4a–c). The key features of these models include: (i) The dominant propagation directions of all wave components are in the wind direction and (ii) the directional beamwidth is narrowest near the spectral peak and becomes broader as the wavelength of an individual spectral component increases or decreases from the peak wavelength. Of these three unimodal directional distribution models, the Donelan et al. distribution is narrower, and the Hasselmann et al. distribution is broader, than the Mitsuyasu et al. distribution. The directional distributions of shorter wave components of the other three models (Banner and Young 1994; Ewans 1998; Hwang et al. 2000b) are bimodal (Figs. 4d–f). As stated earlier, bimodality is a robust feature of nonlinear wave–wave interaction (Banner and Young 1994). The beamwidth (and other similar integrated properties such as directional moments) predicted by the unimodal distributions and the bimodal function (of the ATM results) are shown to be comparable (Hwang et al. 2000b). A brief description of the six directional distribution functions is given in the appendix.

Figures 5a and 5b show the computed $d(k)$ and $r(k_I)$ for a wave field generated by 10 m s^{-1} wind (k and k_I are normalized by k_p in these plots). The rate of increase of $d(k)$ calculated using the bimodal functions are usually larger than those calculated using unimodal directional distributions. Because data from Banner and Young (1994) and Hwang et al. (2000b) are only available to $k/k_p \le 10$, extrapolation to higher wavenumber components is performed. The procedure is described in the appendix.

The integrated ratio, $r(k_I)$, based on bimodal functions is apparently much closer to the observed value. For this wind speed (10 m s^{-1}), $k_s = 214k_p$, and $r(k_s) \approx 0.9$, 0.79, and 0.81 for Ewans (1998), Banner and Young (1994), and Hwang et al. (2000b), respectively. In contrast, $r(k_s)$ is approximately 0.7 based on the models of Mitsuyasu et al. (1975) and Hasselmann et al. (1980), and is less than 0.6 based on the model of Donelan et al. (1985).

The ratio $r(k_s)$ as a function of wind speed is plotted in Fig. 5c. For comparison, the field data of Cox and Munk (1954) are also shown. Of the six directional models, the results of the unimodal directional functions underpredict the ratio considerably. Results from bimodal directional distribution functions can produce the ratio at a level comparable to the observations reported by Cox and Munk (1954). The average ratios and standard deviations of field data and six model functions are shown in Table 2. The results based on bimodal directional distribution are in better agreement with the field data. The agreement of the trends with respect to

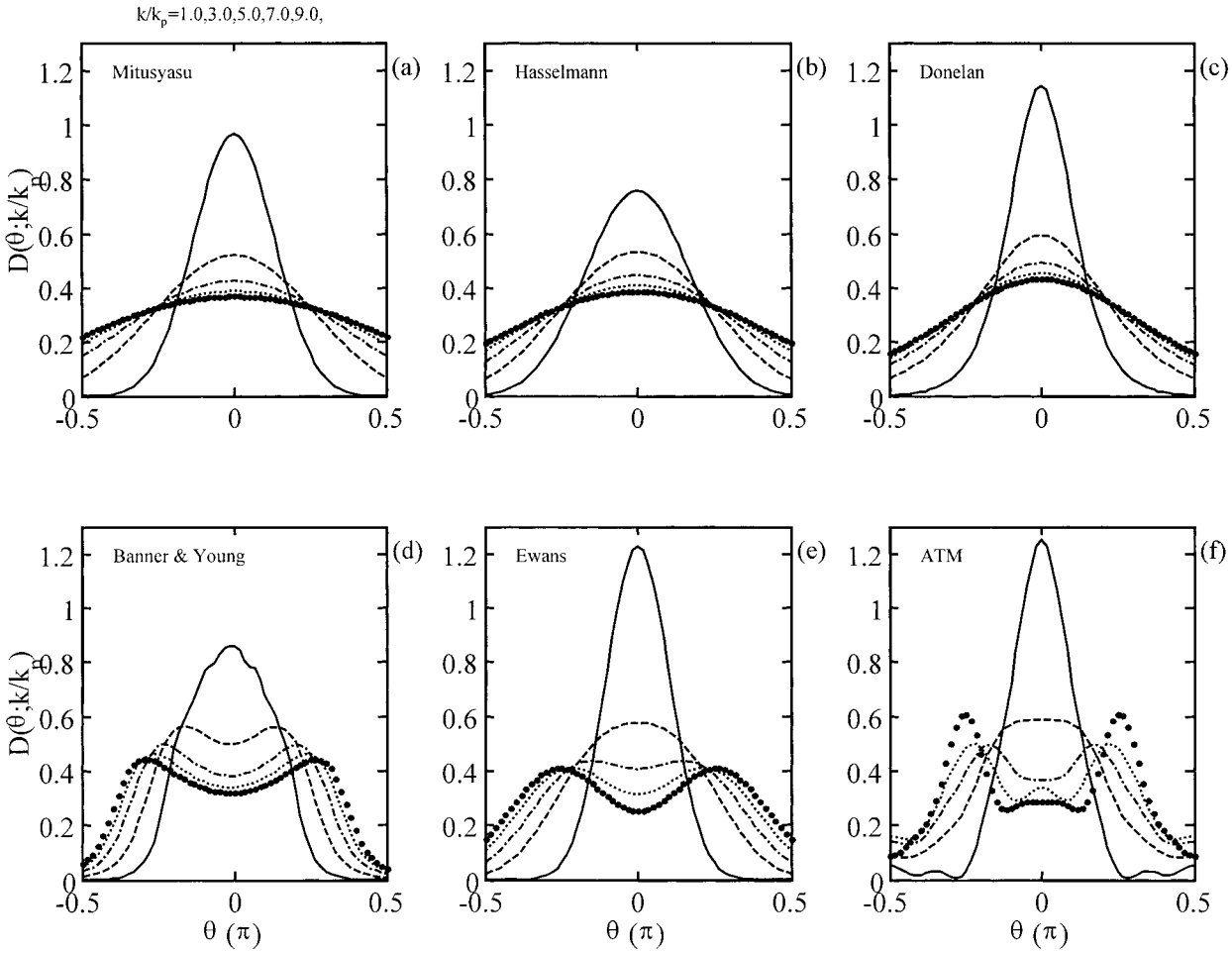

FIG. 4. Directional distribution models of (a) Mitsuyasu et al. (1975), (b) Hasselmann et al. (1980), (c) Donelan et al. (1985), (d) Banner and Young (1994), (e) Ewans (1998), and (f) Hwang et al. (2000b) at $k/k_p = 1$ (solid curves), 3 (dashed curves), 5 (dashed–dotted curves), 7 (dotted curves), and 9 (heavy dots).

the wind speed (Fig. 5c) between field data and model functions remains not very satisfactory. In particular, it is found that for the lower wind speed range, the upwind to crosswind ratio of the mean square slope components in the field data is considerably higher than all model computations. Possible reasons for this result are discussed in the next section.

5. Discussions

a. Spectral function

As mentioned in section 3, although field measurements strongly endorse an equilibrium spectral function with the spectral density increasing in linear proportion to the wind friction velocity and a -2.5 slope of the wavenumber spectrum (8), the range of the equilibrium spectrum remains unknown. Phillips (1985) considers that the upper-limit wavenumber of the equilibrium range is dictated by blockage and suppression of short waves by surface drift currents (9). This upper limit is found to be unusually high. As a result, the integrated mean square slope is several times higher than the field data. Furthermore the integrated mean square slope is independent of wind speed, also in contradiction to field observations.

It is suggested that an equilibrium spectrum (8) soon changes to a saturation spectrum (6). The transition wavenumber is calculated to be in the neighborhood of $(6.5 \pm 2)k_p$. In terms of the wave frequency, the transition frequency f_i is approximately $(2.5 \pm 0.5)f_p$. Many frequency spectra measured in the field also show spectral slopes transitioning from -4 to -5, which are the frequency spectral slopes in the equilibrium and saturation ranges, respectively. It is worth noting that the dimensionless frequency bandwidth of the equilibrium range in some of the reported spectra is also close to 2.5 (e.g., Forristall 1981).

From a different point of view, let us assume that a change of the spectral slope from one range to the other is an indication that the dynamic processes in

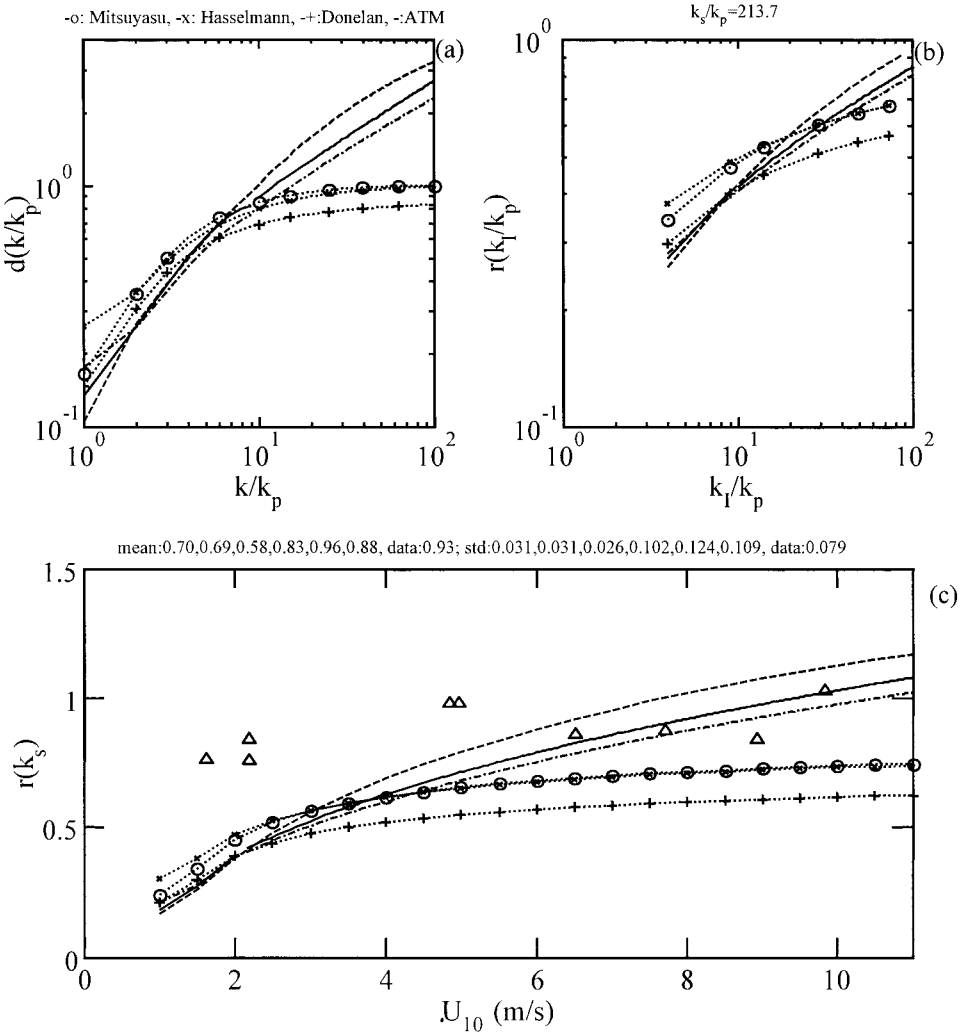

FIG. 5. The ratios (a) $d(k)$ and (b) $r(k_l)$ calculated for a wave field generated by a 10 m s^{-1} wind. (c) The ratio $r(k_s)$ as a function of wind speed. The results of slick cases of Cox and Munk (1954) are also shown as triangles in the plot. Six different directional distribution models are used in the calculation from connected circles: Mitsuyasu et al. (1975); connected crosses: Hasselmann et al. (1980); connected pluses: Donelan et al. (1985), dashed-and-dotted curves: Banner and Young (1994), dashed curves: Ewans (1998), dotted curves: Ewans (1998) with the directional distribution in the high wavenumber range ($k/k_p > 25$) fixed to that at $k/k_p = 25$, and solid curves: Hwang et al. (2000b).

TABLE 2. The mean and standard deviation of the ratio between crosswind and upwind mean square slope components (statistics for three wind-speed ranges are shown).

	Wind speed range (m s^1)		
Source ↓	$1 \le U_{10} \le 10$ Mean (std dev)	$U_{10} < 4$ Mean (std dev)	$4 \le U_{10} \le 10$ Mean (std dev)
Cox and Munk (1954) data	0.88 (0.10)	0.78 (0.05)	0.93 (0.08)
Mitsuyasu et al. (1975)	0.62 (0.14)	0.45 (0.14)	0.70 (0.03)
Hasselmann et al. (1980)	0.62 (0.12)	0.47 (0.11)	0.69 (0.03)
Donelan et al. (1985)	0.52 (0.11)	0.39 (0.11)	0.58 (0.03)
Banner and Young (1994)	0.78 (0.16)	0.48 (0.10)	0.83 (0.10)
Ewans (1998)	0.77 (0.29)	0.41 (0.18)	0.96 (0.12)
Hwang et al. (2000b)	0.82 (0.18)	0.49 (0.11)	0.88 (0.11)

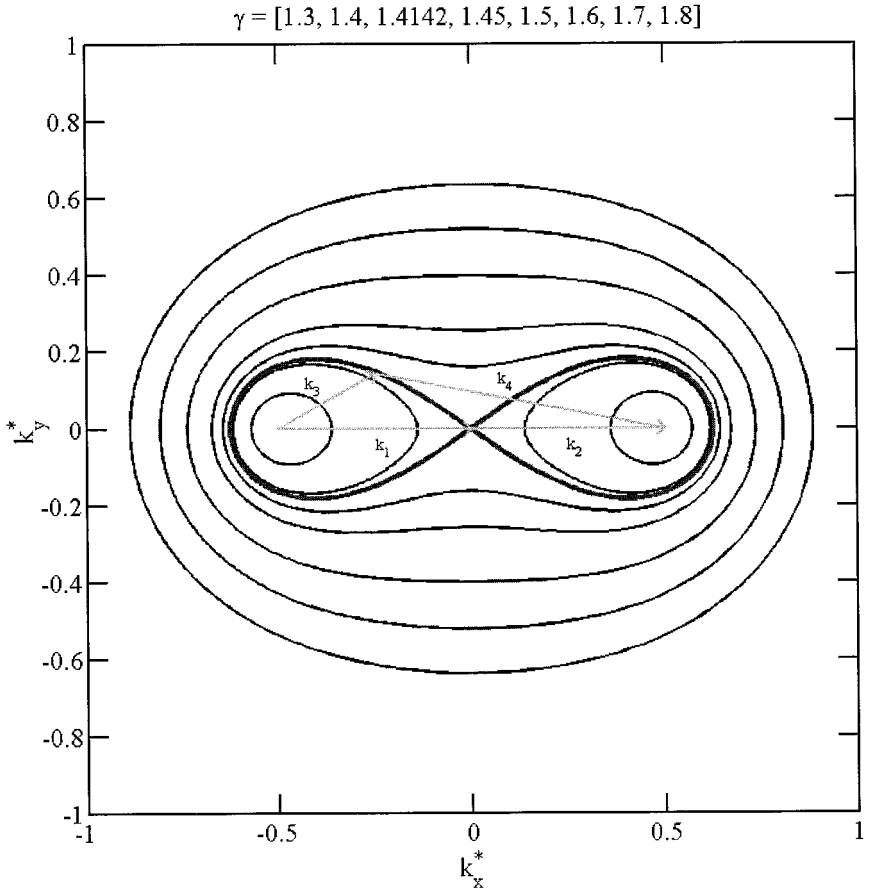

FIG. 6. The family of curves formed by nonlinear interaction quartets, calculated using the solution technique of Young and Van Vledder (1993).

the two ranges have changed. Phillips (1985) gives extensive discussions on the spectral properties in the gravity band above the spectral peak wavenumber. It is assumed that in the region, all three major source functions (wind input, breaking dissipation, and nonlinear wave–wave interaction) exert significant influences on the dynamics of wave evolution. This region is identified as the equilibrium range. The characteristics of the equilibrium spectrum include a (wavenumber) spectral slope of -2.5 and the spectral density is proportional to the wind friction velocity (8). It remains unknown what is the wavenumber range where wind input or wave breaking is active. On the other hand, the theoretical understanding of nonlinear wave–wave interaction is much more mature, and we can have a quantitative estimation of the wavenumber range influenced by the nonlinear interaction mechanism. Figure 6 shows the family of curves of the wavenumber components forming resonant quartets in the gravity wave region, constructed using the solution technique described by Young and Van Vledder (1993). Using the set of curves calculated over the range of γ from 1.1 to 1.9 (Young and Van Vledder 1993, p. 507), the population of the wavenumber vectors forming the resonant quartets are collected and plotted in Fig. 7a, representing the probability distribution of the wavenumber vectors participating in nonlinear wave–wave interaction. For reference, the thick line (the Fig. 8 curve) in the middle of the family of curves (Fig. 6) is the basis for the discrete interaction approximation (DIA) algorithm used in most operational nonlinear wave models such as WAM (Wave Model) and SWAN (Simulating Wave Nearshore). The population of interacting quartets on the (extended) DIA curve, representing the distribution of wave vectors participating in nonlinear interaction with the peak wavenumber component in a given propagation direction, is shown as the continuous line in Fig. 7a. Both sets of computations show a large population density near $2k_p$. The average wavenumber as a function of propagation direction is plotted in Fig. 7b. From this figure, it is seen that interacting quartets with $k > k_p$ are confined within the angular range of $|\theta| \leq 50°$ for $1.1 \leq \gamma \leq 1.9$, and $|\theta| \leq 15°$ for the DIA curve. Because quartet interaction is a third order process, the higher-order moments of the pdf are also calculated. Conceptually, the third moment can be considered as the representative pop-

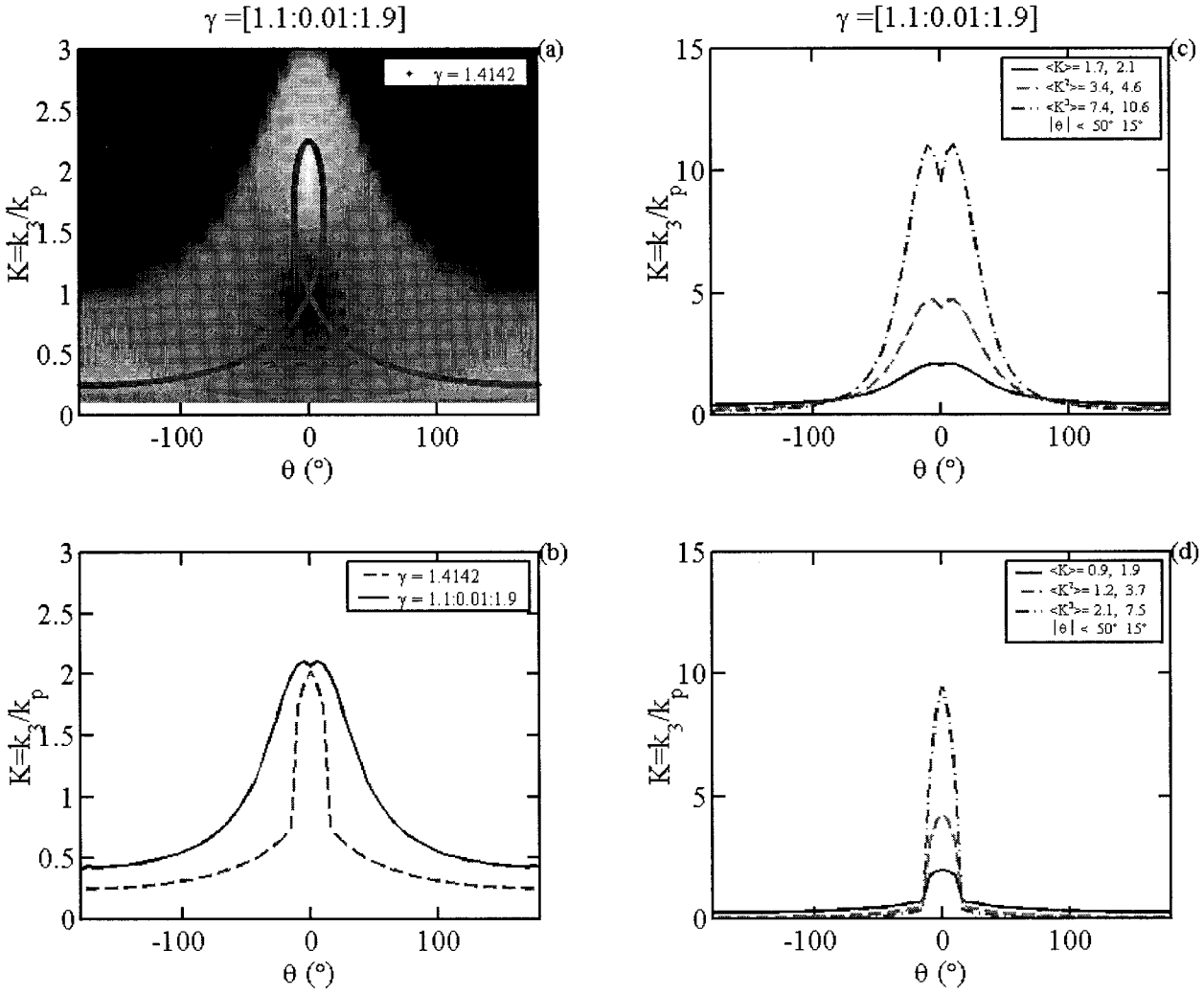

FIG. 7. (a) The probability distribution of the wavenumber vectors that participate in nonlinear interaction. The gray scale image represents computations with $1 \leq \gamma \leq 1.9$. The continuous line is for the DIA curve. (b) The average wavenumber of (a). The solid line is for computations with $1 \leq \gamma \leq 1.9$, the dashed line is from the DIA curve. (c) The first three moments (solid, dashed, and dashed–dotted curves for the first, second, and third moments, respectively) of the probability distribution shown in (a) for the curves corresponding to $1.1 \leq \gamma \leq 1.9$. (d) Same as (c) but for the DIA curve.

ulation of wave components following three cascades of nonlinear interactions involving the peak wavenumber, which represents the primary source of spectral energy feeding into the interacting components. The results for the range $1.1 \leq \gamma \leq 1.9$ are shown in Fig. 7c. The average of the third moment integrated over a directional beamwidth of 50° is 7.4. The results calculated using only the DIA curve are plotted in Fig. 7d. The average of the third moment integrated over a directional beamwidth of 15° is 7.5. It is probably not a coincidence that the calculated range of influence of nonlinear wave–wave interaction in the gravity wave field (a third-order process) is close to the value ($k_i/k_p = 6.5 \pm 2$) where the spectrum changes from an equilibrium form to a saturation form.

b. Directional distribution

As shown in the last section, the crosswind to upwind ratios of mean square slopes calculated using bimodal directional distributions is able to explain the large ratio of the field data (Cox and Munk 1954). As shown in Fig. 5c, in the lower wind speed range, the crosswind to upwind ratio in the field data is considerably higher than all model computations. Several factors may contribute to the observed larger crosswind surface slope component in the ocean. First, the computation is based on the assumption of steady wind forcing. Fluctuations in the wind field, especially the wind direction, may contribute significantly to a higher magnitude of $r(k_s)$. Second, the derivation of the bimodal directional function is based on data from a mature wave field where

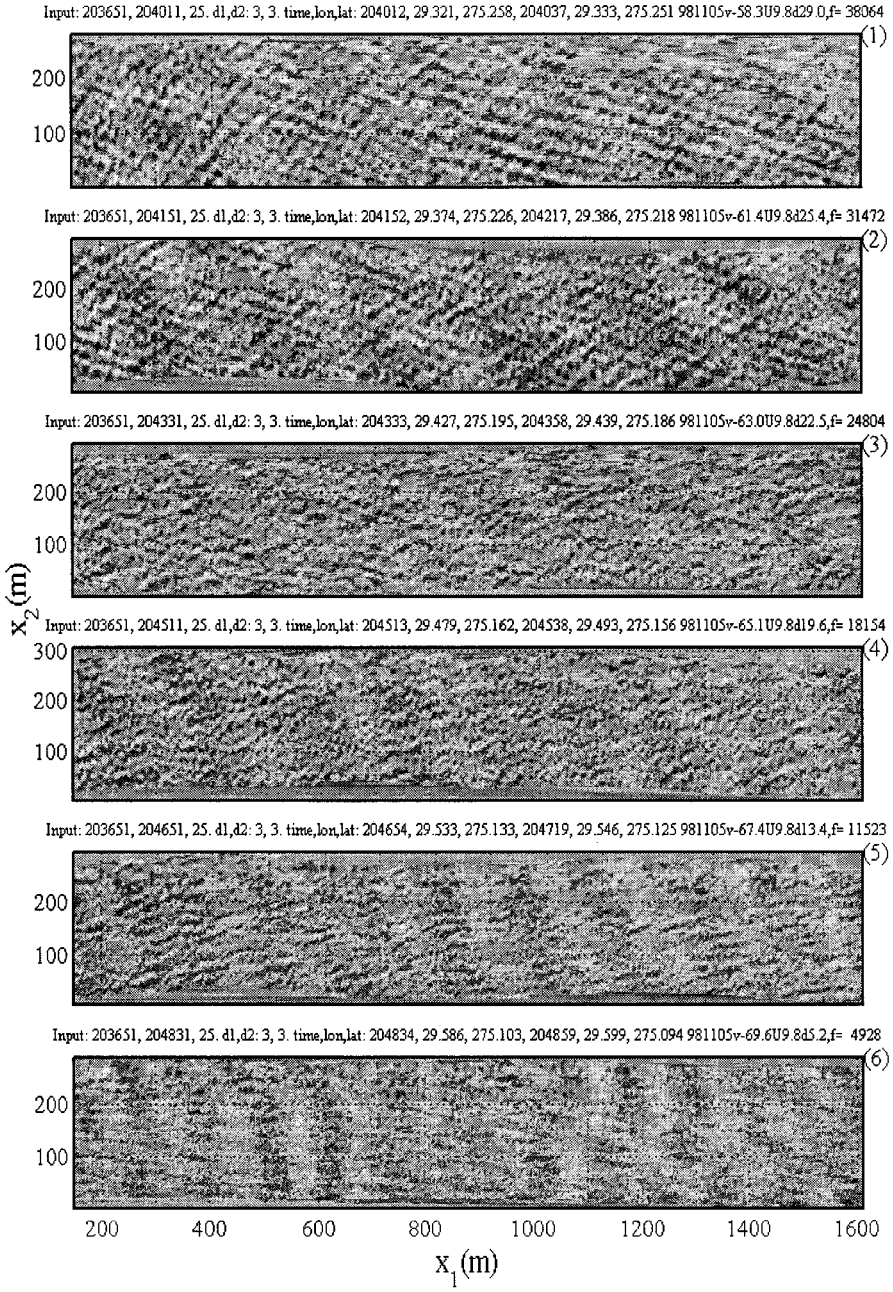

FIG. 8. Examples of the surface wave topography at six different fetches. Wind is from right to left (offshore fetch growth condition). The fetches for the six images are 38.1, 31.5, 24.8, 18.2, 11.5, and 4.9 km from top to bottom.

the dominant wave component aligns with the wind vector. In a young sea, the dominant wave may propagate at oblique angles with respect to the wind vector in order for the wave field to maintain a resonant condition with the forcing wind field. According to the Phillips (1957) resonance mechanism of wind wave generation, two wave systems propagating at oblique angles symmetric to the wind are generated. Spatial measurements of 3D ocean surface topography using airborne scanning radar (Walsh et al. 1985, 1989) and airborne scanning lidar (Hwang et al. 2000c) obtained examples of waves propagating at oblique angles with respect to the wind vector under steady wind forcing. In both cases presented by Walsh et al. (1985, 1989), most of the reported directional spectra have one wind-generated wave system. At a short fetch, the direction of the wind–wave system deviates significantly from the wind vector. In the case reported by Hwang et al. (2000c), two wave systems

straddling the wind vector exist. Figure 8 shows a sequence of the surface wave topography along the 42-km groundtrack of the airborne measurements. In the nearshore region the wave fronts are almost parallel to the wind direction, indicating that very young waves are propagating normal to, rather than along, the wind direction. As fetch length increases waves grow longer and higher, the wave direction also changes from normal to wind to oblique to wind. Since the resonance condition admits two solutions for the propagation angles, $\theta_p = \pm\cos^{-1}C_p/U_r$, where U_r is a reference wind speed, two wave systems symmetric to the wind vector are developed. The surface topography displays a rhomboid pattern from the two systems crossing each other (Fig. 8). The directional spectra of these waves show two distinct spectral peaks straddling the wind vector (not shown). The swell condition in the dataset of Hwang et al. (2000c) is much milder than those encountered in Walsh et al. (1985, 1989), and may contribute to the observed difference of two wave systems oblique to wind in Hwang et al. (2000c) and only one in Walsh et al. (1985, 1989). In any case, one expects a significant increase in the ratio between crosswind and upwind mean square slope components when waves are propagating at an oblique angle with respect to wind.

6. Summary

The mean square slope dataset of Cox and Munk (1954) is regarded a masterpiece in the study of ocean surface roughness. It has been used as a major calibration reference in many areas of research, ranging from air–sea interaction and wave dynamics to acoustic and electromagnetic remote sensing applications. One aspect of the dataset that remains quite puzzling over the last half century or so is the large value of the crosswind slope component. For slick covered cases, the ratio between crosswind and upwind mean square slope components ranges from 0.75 to 1.03. The mean value with one standard deviation is 0.88 $\pm$ 0.097. The large crosswind slope component cannot be explained by the unimodal directional functions established in modern wave spectral models (Fig. 5c). The mean ratio from three unimodal directional distribution functions (Donelan et al. 1985, with modification by Banner 1990; Hasselmann et al. 1980; and Mitsuyasu et al. 1975) are 0.54 $\pm$ 0.11, 0.65 $\pm$ 0.12, and 0.65 $\pm$ 0.13, respectively.

Directional spectral analysis of 3D ocean surface topography collected by an airborne scanning lidar system shows that in a mature sea, unimodal directional distribution exists only in a narrow wavenumber range near the spectral peak. For wave components shorter than the dominant wavelength, bimodality is a robust feature of the directional distribution. Nonlinear wave–wave interaction is the mechanism that generates the bimodal feature (Banner and Young 1994). Using the ATM bimodal directional distribution function, the calculated average ratio between crosswind and upwind slope components is 0.88 $\pm$ 0.10. The rate of increase of the ratio with respect to the wind speed in the field data, however, is found to be considerably different from model computations (Fig. 5c). Particularly, in the low wind speed range, the models persistently underestimate the crosswind to upwind ratio. Possible factors contributing to the observed larger crosswind slope components in the field data include fluctuation in the wind field and less-than-mature stage of the wave field. In both situations, wave components traveling at oblique angles from the wind vector make large contribution to the average crosswind slope component.

We also investigated the spectral function above the wave spectral peak. Assuming that the wave spectrum transitions from an equilibrium form to a saturation form, the transition wavenumber is calculated to be in the neighborhood of $k_i/k_p = 6.5 \pm 2$. This number is close to the upper range of the wavenumbers influenced by nonlinear wave–wave interaction. Following the discussions of Phillips (1985), in the equilibrium range wind input, breaking dissipation, and nonlinear interaction are the three major mechanisms shaping the ocean wave spectral function. If a change of the spectral slope from one range to the other is an indication that there is a shift of dynamic processes governing the wave evolution in the two ranges, the results suggest that the contribution of nonlinear interaction in the saturation range is less important. The balance of driving forces in the saturation range is dictated by wind input and breaking dissipation, as originally suggested by Phillips (1958). These results then indicate that the upper end of the equilibrium range is approximately $6.5k_p$, or $2.5f_p$.

Acknowledgments. This work is sponsored by the Office of Naval Research (Naval Research Laboratory research project Phase-Resolved Nonlinear Shoaling Waves, PE62435N).

APPENDIX

Directional Distribution Functions

Six different models of the directional distribution functions are used in the computation presented in this paper. Detailed comparisons of these distribution models have been published elsewhere (e.g., Young 1994; Ewans 1998; Hwang et al. 2000b). This appendix presents a short description of each model.

a. Mitsuyasu et al. (1975)

Using data collected by a cloverleaf buoy, Mitsuyasu et al. (1975) propose the following directional distribution function:

$$D(\omega, \theta) = Q(s)\cos^{2s}\left[\frac{\theta - \theta_m}{2}\right], \qquad \text{(A1)}$$

TABLE A1. Third-order polynomial fitting ($y = c_1x^3 + c_2x^2c_3x + c_4$, where y is $A_1, A_2, \ldots, A_9$, and x is k/k_p) of the Fourier components, $A_1, A_2, \ldots, A_9$, of the bimodal directional distribution (A12).

	c_1	c_2	c_3	c_4
A_1	-6.83×10^{-4}	2.20×10^{-2}	-2.42×10^{-1}	9.87×10^{-1}
A_2	-2.66×10^{-3}	5.32×10^{-2}	-3.82×10^{-1}	7.83×10^{-1}
A_3	-1.44×10^{-3}	3.29×10^{-2}	-2.08×10^{-1}	3.26×10^{-1}
A_4	-1.13×10^{-3}	2.15×10^{-2}	-1.01×10^{-1}	1.17×10^{-1}
A_5	-7.22×10^{-4}	1.09×10^{-2}	-4.70×10^{-2}	5.96×10^{-2}
A_6	-9.04×10^{-4}	1.21×10^{-2}	-4.92×10^{-2}	7.40×10^{-2}
A_7	5.92×10^{-4}	-8.34×10^{-3}	2.75×10^{-2}	-9.78×10^{-3}
A_8	-1.10×10^{-3}	1.57×10^{-2}	-7.13×10^{-2}	9.80×10^{-2}
A_9	4.33×10^{-4}	-5.93×10^{-3}	2.06×10^{-2}	-1.52×10^{-2}

where θ_m is the mean wave direction (of each wave frequency), $Q(s)$ is a normalization factor such that the integration of the directional distribution function equals to one. The parameter s is given by

$$s = \begin{cases} s_p\left(\dfrac{\omega}{\omega_p}\right)^5, & \omega < \omega_p \\ s_p\left(\dfrac{\omega}{\omega_p}\right)^{-2.5}, & \omega \geq \omega_p, \end{cases} \tag{A2}$$

where s_p is the value of s at the spectral peak frequency

$$s_p = 11.5\left(\frac{U_{10}}{C_p}\right)^{-2.5} \tag{A3}$$

and C_p is the phase speed of the wave component at the spectral peak.

b. Hasselmann et al. (1980)

Hasselmann et al. (1980) use wave data collected by pitch-and-roll buoys for their directional analysis. The functional form of their distribution is also cosine to the $2s$ power (A1), with the following modification of the s parameter,

$$s = \begin{cases} 6.97\left(\dfrac{\omega}{\omega_p}\right)^{4.06}, & \omega < 1.05\omega_p \\ 9.77\left(\dfrac{\omega}{\omega_p}\right)^{\mu}, & \omega > 1.05\omega_p, \end{cases} \tag{A4}$$

where

$$\mu = -2.33 - 1.45\left(\frac{U_{10}}{C_p} - 1.17\right). \tag{A5}$$

c. Donelan et al. (1985)

Donelan et al. (1985) use data collected from a 14-element wave gauge array, and propose a different directional function,

$$D(\omega, \theta) = 0.5\beta \operatorname{sech}^2[\beta(\theta - \theta_m)], \tag{A6}$$

where β is related to the directional beamwidth. The noise level in the directional function derived from the wave gauge array data is apparently too large in the high frequency range, $\omega > 1.6\omega_p$. Banner (1990) supplements the parameterization of β at higher frequencies using his stereophotographic data,

$$\beta = \begin{cases} 2.61\left(\dfrac{\omega}{\omega_p}\right)^{1.3}, & 0.56\omega_p < \omega \leq 0.95\omega_p \\ 2.28\left(\dfrac{\omega}{\omega_p}\right)^{-1/3}, & 0.95\omega_p < \omega \leq 1.6\omega_p \\ 10^{\{-0.4+0.893 \exp[-0.567 \ln(\omega^2/\omega_p^2)]\}}, & \omega > 1.6\omega_p. \end{cases} \tag{A7}$$

d. Banner and Young (1994)

Numerical computations show that application of the nonlinear theory results in a bimodal directional spreading. I. Young kindly provided the numerical results of $\chi(k, \theta)$ for one of their simulation cases (Case Y10UT, $U_{10} = 10$ m s^{-1}, unconstrained tail, Table 1 of Banner and Young 1994). The directional distribution of this case is used for the computations shown in Figs. 4 and 5. The range of the spectrum covers $0.2 \leq k/k_p \leq 9.5$ (in steps of 0.2 and 0.5 for $k/k_p \leq 1$ and $k/k_p > 1$, respectively) and $-122.5° \leq \theta \leq 117.5°$ (in steps of

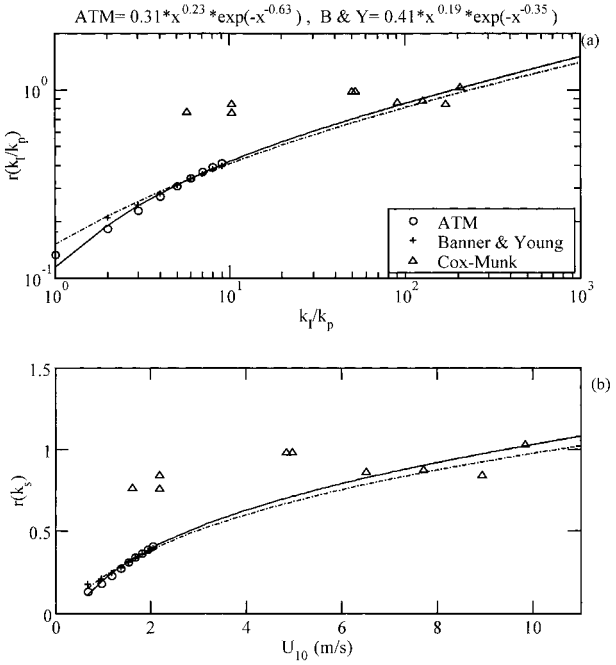

FIG. A1. Extrapolation of the directional distribution functions of Banner and Young (1994, +) and Hwang et al. (2000b, open circle symbol) to the wavenumber components beyond k/k (inferior italic lower case p) = 10. Field data (Cox and Munk 1954, open triangle symbol) are used to guide the nonlinear fitting procedure.

5°). For wave components above $10k_p$, nonlinear curve fitting of the computations from 1 to 9.5 k_p to the lower bound of the Cox and Munk (1954) measurements are used to generate the crosswind to upwind ratio (Fig. A1). The nonlinear fitting function results in the following function:

$$r = \left(\frac{k}{k_p}\right) = 0.41\left(\frac{k}{k_p}\right)^{0.19} \exp\left[-\left(\frac{k}{k_p}\right)^{-0.35}\right]. \quad \text{(A8)}$$

e. Ewans (1998)

Ewans (1998) presents analyses of a one-year-long directional wave measurement program near a Maui platform off the west coast of New Zealand. Cases are carefully selected for steady wind events and offshore fetch growth conditions. The MEM and MLM techniques are used to derive the directional spectrum of the wind waves and the results are used to construct a parametric bimodal directional model combining two Gaussian distribution functions:

$$D(f, \theta) = \frac{1}{\sqrt{8\pi}\sigma(f)} \sum_{n=-\infty}^{\infty} \times \left\{\exp\left[-\frac{1}{2}\left(\frac{\theta - \theta_{m1} - 2\pi n}{\sigma(f)}\right)\right] + \exp\left[-\frac{1}{2}\left(\frac{\theta - \theta_{m2} - 2\pi n}{\sigma(f)}\right)\right]\right\}, \quad \text{(A9)}$$

where $\sigma(f)$ is the angular spreading of each frequency component, and θ_{m1} and θ_{m2} are the locations of the peaks. Assuming symmetric bimodal distribution, $\theta_{m1} = -\theta_{m2}$. Through least square fitting, the spreading function and the peak angle are given by

$$\theta_{m2} = -\theta_{m1} = \begin{cases} \dfrac{14.93}{2}, & f < f_p \\ \dfrac{1}{2}\exp\left[5.453 - 2.750\left(\dfrac{f}{f_p}\right)^{-1}\right], & f \geq f_p \end{cases} \quad \text{(A10)}$$

and

$$\sigma(f) = \begin{cases} 11.38 - 5.357\left(\dfrac{f}{f_p}\right)^{-7.929}, & f < f_p \\ 32.13 - 15.39\left(\dfrac{f}{f_p}\right)^{-2}, & f \geq f_p. \end{cases} \quad \text{(A11)}$$

f. Hwang et al. (2000b)

Hwang et al. (2000b) acquire the 3D ocean surface topography using an airborne scanning lidar system. Based on data obtained under a quasi-steady wind field the directional distribution function at each wavenumber of the measured 2D spectrum is expressed in Fourier series,

$$D(k, \theta) = \frac{1}{\pi}\left[1 + 2\sum_{n=1}^{N} A_n(k)\cos 2n\theta\right], \quad -\pi/2 \leq \theta \leq \pi/2. \quad \text{(A12)}$$

[Note: The factor of 2 in the Fourier coefficients is missing in Eqs. (7) and (8) of Hwang et al. (2000). Coefficients for the third order polynomial fitting to each of the first nine Fourier components, A_n, $n = 1, 2, \cdots, 9$, are tabulated for reconstructing the bimodal function (Table A1). The database that establishes the polynomial coefficients is limited to $k \leq 10k_p$, so extrapolation too far beyond $10k_p$ may produce large excursions in the directional function. For wave components above $10k_p$, nonlinear curve fitting of the computations from 1 to 10 k_p to the lower bound of the Cox and Munk (1954) measurements are used to generate the crosswind to upwind ratio (Fig. A1). The nonlinear fitting function results in the following function:

$$r\left(\frac{k}{k_p}\right) = 0.31\left(\frac{k}{k_p}\right)^{0.23} \exp\left[-\left(\frac{k}{k_p}\right)^{-0.63}\right]. \quad \text{(A13)}$$

REFERENCES

Banner, M. L., 1990: Equilibrium spectra of wind waves. *J. Phys. Oceanogr.*, **20,** 966–984.
——, and I. R. Young, 1994: Modeling spectral dissipation in the

evolution of wind waves. Part I: Assessment of existing model performance. *J. Phys. Oceanogr.,* **24,** 1550–1571.

Bock, E. J., and T. Hara, 1995: Optical measurements of capillary–gravity wave spectra using a scanning laser slope gauge. *J. Atmos. Oceanic Technol.,* **12,** 395–403.

Cote, L. J., and Coauthors, 1960: The directional spectrum of a wind generated sea as determined from data obtained by the Stereo Wave Observation Project. *Meteor. Papers,* Vol. 2, New York University, 88 pp.

Cox, C. S., and W. Munk, 1954: Statistics of the sea surface derived from sun glitter. *J. Mar. Res.,* **13,** 198–227.

Donelan, M. A., 1990: Air–sea interaction. *The Sea. Vol. 9: Ocean Engineering Science,* B. LeMehaute and D. M. Hanes, Eds., Wiley and Sons, 239–292.

——, J. Hamilton, and W. H. Hui, 1985: Directional spectra of wind-generated waves. *Philos. Trans. Roy. Soc. London,* **A315,** 509–562.

——, W. M. Drennan, and E. A. Terray, 1999: Wavenumber spectra of wind waves in the range of 1–50 m. *The Wind-Driven Air–Sea Interface,* M. L. Banner, Ed., ADFA Document Production Center, 35–42.

Ewans, K. C., 1998: Observations of the directional spectrum of fetch-limited waves. *J. Phys. Oceanogr.,* **28,** 495–512.

Forristall, G. Z., 1981: Measurements of a saturated range in ocean wave spectra. *J. Geophys. Res.,* **86,** 8075–8084.

Hara, T., E. J. Bock, and D. Lyzenga, 1994: In situ measurements of capillary–gravity wave spectra using a scanning laser slope gauge and microwave radars. *J. Geophys. Res.,* **99,** 12 593–12 602.

——, ——, J. Edson, and W. McGillis, 1998: Observation of short wind waves in coastal waters. *J. Phys. Oceanogr.,* **28,** 1425–1438.

Hasselmann, D. E., M. Dunckel, and J. A. Ewing, 1980: Directional wave spectra observed during JONSWAP 1973. *J. Phys. Oceanogr.,* **10,** 1264–1280.

Hasselmann, K., and Coauthors, 1973: Measurements of wind wave growth and swell decay during the Joint North Sea Wave Project (JONSWAP). *Dtsch. Hydrogr. Z.,* **8A** (Suppl.), 95 pp.

Holthuijsen, L. H., 1983: Observations of the directional distribution of ocean-wave energy in fetch-limited conditions. *J. Phys. Oceanogr.,* **13,** 191–207.

Hughes, B. A., H. L. Grant, and R. W. Chappell, 1977: A fast response surface-wave slope meter and measured wind-wave moment. *Deep-Sea Res.,* **24,** 1211–1223.

Hwang, P. A., 1995: Spatial measurements of small-scale ocean waves. *Air–Water Gas Transfer,* B. Jahne and E. C. Monahan, Eds., AEON Verlag and Studio, 153–164.

——, 1997: A study of the wavenumber spectra of short water waves in the ocean. Part II: Spectral model and mean square slope. *J. Atmos. Oceanic Technol.,* **14,** 1174–1186.

——, and O. H. Shemdin, 1988: The dependence of sea surface slope on atmospheric stability and swell condition. *J. Geophys. Res.,* **93,** 13 903–13 912.

——, S. Atakturk, M. A. Sletten, and D. B. Trizna, 1996: A study of the wavenumber spectra of short water waves in the ocean. *J. Phys. Oceanogr.,* **26,** 1266–1285.

——, D. W. Wang, E. J. Walsh, W. B. Krabill, and R. N. Swift, 2000a: Airborne measurements of the wavenumber spectra of ocean surface waves. Part I: Spectral slope and dimensionless spectral coefficient. *J. Phys. Oceanogr.,* **30,** 2753–2767.

——, ——, ——, ——, and ——, 2000b: Airborne measurements of the wavenumber spectra of ocean surface waves. Part II: Directional distribution. *J. Phys. Oceanogr.,* **30,** 2768–2787.

——, ——, W. B. Krabill, W. Wright, and R. N. Swift, 2000c: Evolution of the directional distribution of a fetch-limited wave field. *Proc. Sixth Int. Workshop on Wave Hindcasting and Forecasting,* in press.

Jackson, F. C., W. T. Walton, and C. Y. Peng, 1985: A comparison of in situ and airborne radar observations of ocean wave directionality. *J. Geophys. Res.,* **90,** 1005–1018.

Klinke, J., and B. Jahne, 1995: Measurements of short ocean waves during the MBL ARI West Coast Experiment. *Air–Water Gas Transfer,* B. Jahne and E. C. Monahan, Eds., AEON Verlag and Studio, 165–173.

Longuet-Higgins, M. S., D. E. Cartwright, and N. D. Smith, 1963: Observations of the directional spectrum of sea waves using the motions of a floating buoy. *Ocean Wave Spectra,* Prentice-Hall, 111–136.

Mitsuyasu, H., F. Tasai, T. Suhara, S. Mizuno, M. Ohkusu, T. Honda, and K. Rikiishi, 1975: Observation of the directional wave spectra of ocean waves using a cloverleaf buoy. *J. Phys. Oceanogr.,* **5,** 750–760.

Phillips, O. M., 1957: On the generation of waves by turbulent wind. *J. Fluid Mech.,* **2,** 417–445.

——, 1958: On some properties of the spectrum of wind-generated ocean waves. *J. Mar. Res.,* **16,** 231–240.

——, 1977: *The Dynamics of the Upper Ocean.* 2d ed. Cambridge University Press.

——, 1985: Spectral and statistical properties of the equilibrium range in wind-generated gravity waves. *J. Fluid Mech.,* **156,** 505–531.

Tang, S., and O. H. Shemdin, 1983: Measurement of high frequency waves using a wave follower. *J. Geophys. Res.,* **88,** 9832–9840.

Walsh, E. J., D. W. Hancock, D. E. Hines, R. N. Swift, and J. F. Scott, 1985: Directional wave spectra measured with the surface contour radar. *J. Phys. Oceanogr.,* **15,** 566–592.

——, ——, ——, ——, and ——, 1989: An observation of the directional wave spectrum evolution from shoreline to fully developed. *J. Phys. Oceanogr.,* **19,** 670–690.

Wang, D. W., and P. A. Hwang, 2001: Evolution of the bimodal directional distribution of ocean waves. *J. Phys. Oceanogr.,* **31,** 1200–1221.

Wyatt, L. R., 1995: The effect of fetch on the directional spectrum of Celtic Sea storm waves. *J. Phys. Oceanogr.,* **25,** 1550–1559.

Wu, J., 1982: Wind-stress coefficients over sea surface from breeze to hurricane. *J. Geophys. Res.,* **87,** 9704–9706.

Young, I. R., 1994: On the measurement of directional wave spectra. *Appl. Ocean Res.,* **16,** 283–294.

——, and G. Ph. Van Vledder, 1993: A review of the central role of nonlinear interactions in wind-wave evolution. *Philos. Trans. Roy. Soc. London,* **A342,** 505–524.

——, L. A. Verhagen, and M. L. Banner, 1995: A note on the bimodal directional spreading of fetch-limited wind waves. *J. Geophys. Res.,* **100,** 773–778.